Heliyon 10 (2024) e33154

Contents lists available at ScienceDirect

Heliyon

journal homepage: www.cell.com/heliyon

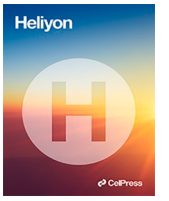

Research article

Potential preventative impact of aloe-emodin nanoparticles on cerebral stroke-associated myocardial injury by targeting myeloperoxidase: In supporting with *In silico* and *In vivo* studies

Praveen Kumar Pasala [a], Niranjan Kumar Raghupathi [b], Deepak A. Yaraguppi [c], Ranadheer Reddy Challa [d], Bhaskar Vallamkonda [e], Sheikh F. Ahmad [f], Yeswanth Chennamsetty [b], P.V. Kamala Kumari [g], Prasanth DSNBK [h,*]

[a] *Department of Pharmacology, Raghavendra Institute of Pharmaceutical Education and Research, JNTUA, Anantapuramu, Andhra Pradesh, 515721, India*
[b] *Department of Pharmacology, Santhiram College of Pharmacy, JNTUA, Nandyal, 518112, Andhra Pradesh, India*
[c] *Department of Biotechnology, KLE Technological University, Hubli, Karnataka, 580031, India*
[d] *Department of Formulation and Development, Quotient Sciences, 3080 McCann Farm Dr, Garnet Valley, PA, 19060, USA*
[e] *Department of Pharmaceutical Analysis, Odin Pharmaceutical LLC, Somerset, NJ, 08873, USA*
[f] *Department of Pharmacology and Toxicology, College of Pharmacy, King Saud University, Riyadh, 11451, Saudi Arabia*
[g] *Department of Pharmaceutics, Vignan Institute of Pharmaceutical Technology, Duvvada, Visakhapatnam, India*
[h] *School of Pharmacy & Technology Management, SVKM's Narsee Monjee Institute of Management Studies (NMIMS), Polepally SEZ, TSIIC, Jadcherla, Mahbubnagar, Hyderabad, 509301, India*

ARTICLE INFO

Keywords:
Aloe emodin
Aloe emodin nanoparticles
Myeloperoxidase
Antioxidant
Molecular dynamics
Molecular docking

ABSTRACT

The present study examined the potential neuroprotective effects of aloe-emodin (AE) nanoparticles on the cerebral stroke-associated target protein myeloperoxidase (MPO). We investigated the binding interactions between AE and MPO through molecular docking and molecular dynamics simulations. Molecular docking results indicated that AE exhibited a binding energy of −6.9 kcal/mol, whereas it was −7.7 kcal/mol for 2-{[3,5-bis(trifluoromethyl)benzyl]amino}-*n*-hydroxy-6-oxo-1,6-dihydropyrimidine-5-carboxamide (CCl). Furthermore, molecular dynamics studies demonstrated that AE possesses a stronger binding affinity (−57.137 ± 13.198 kJ/mol) than does CCl (−22.793 ± 30.727 kJ/mol), suggesting that AE has a more substantial inhibitory effect on MPO than does CCl. Despite the therapeutic potential of AE for neurodegenerative disorders, its bioavailability is limited within the body. A proposed hypothesis to enhance the bioavailability of AE is its conversion into aloe-emodin nanoparticles (AENP). The AENPs synthesized through a fabrication method were spherical with a consistent diameter of 104.4 ± 7.9 nm and a polydispersity index ranging from 0.525 to 0.586. In rats experiencing cerebral stroke, there was a notable increase in cerebral infarction size; abnormalities in electrocardiogram (ECG) and electroencephalogram (EEG) patterns; a decrease in brain and cardiac antioxidant activities; and an increase in myeloperoxidase levels compared to those in normal rats. Compared with AE treatment, AENP treatment significantly ameliorated cerebral infarction, normalized ECG and EEG patterns, enhanced brain and cardiac antioxidant activities, and reduced MPO levels in stroke rats. Histopathological evaluations revealed pronounced alterations in the rat hippocampus, with pyknotic nuclei, disarray and loosely packed cells, deterioration of cardiac muscle

* Corresponding author.
E-mail addresses: dsnbkprasanth@gmail.com, dsnbk.prasanth@nmims.edu (P. DSNBK).

https://doi.org/10.1016/j.heliyon.2024.e33154
Received 28 March 2024; Received in revised form 6 June 2024; Accepted 14 June 2024
Available online 15 June 2024

fibers, and extensive damage to cardiac myocytes, in contrast to those in normal rats. AENP treatment mitigated these pathological changes more effectively than AE treatment in both brain and cardiac cells. These findings support that AENP provides considerable protection against stroke-associated myocardial infarction.

1. Introduction

Oxidative stress is a predominant pathophysiological contributor to cerebral stroke, exacerbating neurological damage and inciting systemic complications, including myocardial injury. The abrupt suspension and subsequent reestablishment of blood flow during cerebral ischemic events give rise to the generation of reactive oxygen species (ROS). Excessive ROS production during cerebral I/R injury causes cellular and molecular oxidative injury, exacerbating both cardiac and cerebral tissue damage [1]. ROS play a pivotal role in coordinating several deleterious processes that contribute to lipid peroxidation, DNA fragmentation and protein oxidation and preferentially damage highly oxygenated cells [2,3]. Oxidative events observed in myocardial tissues after stroke have been associated with arrhythmogenesis, depressed contractility and myocardial remodeling, highlighting the profound effect that cerebral events have on cardiac function and vice versa [4,5]. Similarly, oxidative stress markers such as malondialdehyde (MDA) and myeloperoxidase (MPO) are commonly increased after stroke, paralleling the severity of cardiac involvement, possibly reflecting an inflammatory response to both cardiac and cerebral injury [6,7]. Antioxidant defense systems such as those involving innate enzymes, including superoxide dismutase (SOD) and glutathione peroxidase, are also impaired during cerebral I/R, resulting in a systemic oxidative stress response [8]. In summary, the available data emphasize the central role of oxidative stress in the development of myocardial injury after stroke, identifying a therapeutic target to alleviate exacerbated complications after stroke.

MPO is recognized as a pivotal enzyme in the pathology of cerebral stroke-associated myocardial injury and serves as a critical link between inflammatory pathways and oxidative tissue damage [9]. There is a well-documented increase in the expression and activity of MPO within the ischemic myocardium, indicating its role in intensifying poststroke cardiac complications. The role of the enzyme in generating reactive oxygen species and activating inflammatory cascades highlights the destructive interaction between cerebral incidents and secondary organ damage [10]. Initial studies lent empirical support to the involvement of MPO in myocardial harm, wherein the therapeutic inhibition of MPO resulted in reduced oxidative stress markers and decreased cardiac injury after ischemic stroke [11]. Subsequent molecular research has reinforced the significance of MPO as a therapeutic target, demonstrating that a decrease in MPO activity correlates with a diminished degree of damage in cardiac tissue in preclinical stroke models.

Aloe-emodin (AE), a naturally occurring anthraquinone derived from the Aloe species, has garnered attention in pharmacological research due to its broad spectrum of therapeutic properties. It has been reported to possess potential pharmacological activities, including cardioprotective [12], antifungal [13], anticancer [14], antiviral [14], anti-liver fibrosis [15], immunosuppressive [16], cerebroprotective [17], hepatoprotective [18], antiplasmodial [16], and anti-atherosclerotic [19] effects. Unfortunately, because of its remarkable neuroprotective potential, the clinical application of AE is hindered by several pharmacological challenges, notably, its low water solubility, poor absorption and extremely low systemic bioavailability, which restrains its bioavailability in the bloodstream and target organs. As demonstrated in several therapeutic studies, the poor bioavailability of AE can be ascribed to its fast metabolism and excretion, as well as to its poor membrane permeability [20,21]. In an attempt to overcome such limitations, recent advances in nanoscience and nanotechnology have led to the emergence of innovative drug delivery systems [22,23]. The use of nanotechnology-aided formulations of AEs as nanoparticles (AENPs) has gained momentum and been considered by many research groups [24]. Due to their unique features, which include enhanced solubility and stability, enhanced permeability across biological barriers and improved retention in systemic circulation, AENPs have the potential to amplify the cerebroprotective and cardioprotective effects of AE. Thus, it can be suggested that this drug formulation can significantly improve the delivery of AE to the brain and myocardial tissues and thereby dramatically enhance its therapeutic efficacy. MPO is a crucial enzyme involved in inflammation and a target for therapeutic intervention. It has a role in both oxidative stress and neuroinflammation during the development of cerebral ischemia–reperfusion injury [25]. Current inhibitors of MPO that have been explored for the treatment of cerebral stroke and myocardial infarction include compounds such as 4-aminobenzoic acid hydrazide and thioxanthines, which have demonstrated efficacy in reducing MPO activity and related tissue damage [26–28]. Park MY et al. [29] reported that AE reduces the expression of COX2 and INOS during inflammation. However, there is currently no scientific evidence supporting the idea that aloe emodin inhibits inflammation and oxidative stress by inhibiting MPO. Therefore, the current study focused on integrating experimental findings with computational models to improve our understanding of the molecular dynamics that facilitate the beneficial effects of AE and its interplay with pivotal inflammatory mediators such as MPO and to evaluate MPO expression in the brain and heart tissue of stroke rats.

2. Materials and methods

2.1. Materials

Aloe-emodin (AVRA Synthesis Pvt. In addition, Hyderabad, CAS Number: 481-72-1), DTNB (5,5-dithiol-bis-(2-nitrobenzoic acid) (Kemphasol, Mumbai, Maharashtra; CAS Number: 69-78-3), 2,3,5-triphenyl tetrazolium chloride (TTC) (Suvidhinath Laboratories, Vadodara, Gujarat; CAS Number: 298-96-4), phenazine methosulfate (TCI Pvt. Ltd., CAS Number 299-11-6), nitro blue tetrazolium

chloride (SRL Pvt. Ltd., India, CAS Number 298-83-9), β-nicotinamide adenine dinucleotide disodium salt (SRL Pvt. Ltd. India, CAS Number 606-68-8)

2.2. In silico studies

2.2.1. Protein preparation

The 3D structure of MPO in complex with the reversible inhibitor HX1 (PDB ID: 4C1M) [30] was downloaded from the Protein Data Bank (PDB). All nonprotein molecules were excluded from 4C1M. All docking calculations were performed using AutoDock 4.0 [31]. MPO was modified by endowing it with polar hydrogen and performing rigid-body docking in AutoDock. In contrast, all torsional bonds of the ligands were set free using AutoDock Tools.

2.2.2. Ligand preparation

The 2D structures of the ligands AE (https://pubchem.ncbi.nlm.nih.gov/compound/10207) and CCl (2-{[3,5-bis(trifluoromethyl) benzyl]amino}-*n*-hydroxy-6-oxo-1,6-dihydropyrimidine-5-carboxamide) were obtained from PubChem. The ligands were then docked with the force field MMFF94 and converted into a 3D structure [32].

2.2.3. Molecular docking

A docking study was performed using AutoDock Vina [31]. The input files needed to run this program were prepared using AutoDock software. The AutoDock files were prepared by adding polar hydrogen atoms and Gasteiger charges. For X, Y, and Z, the grid box size in AutoDock Vina was maintained at 12, and the binding center was located at x = 17.942000, y = −19.690519 and z = −2.558926. However, the default setting maintained the energy range at eight. AutoDock Vina developers have provided a shell script for implementing Vina [33]. Ligand-binding affinity was expressed as a negative score, with kcal/mol as a unit. Each ligand input generated nine ligand poses with different binding energies, similar to the AutoDock Vina script. The pose with the highest binding affinity was extracted from the docked complex using an in-house Perl script.

2.2.4. Molecular dynamics

Myeloperoxidase was selected as the target molecule for studies with the reversible inhibitor HX1 (PDB ID: 4C1M). Both AE and CCl {2-{[3,5-bis(trifluoromethyl)benzyl]amino}-N-hydroxy-6-oxo-1,6-dihydropyrimidine-5-carboxamide} were chosen for molecular dynamics (MD) simulations. The ligand topology was generated using the ATB server [34]. The GROMACS tool pdb2gmx was utilized to add hydrogen atoms to the heavy atoms of the ligands. Initially, the energy of the prepared systems was minimized under vacuum by employing 1500 steepest descent steps. Following energy minimization, the systems were solvated in a cubic periodic box using the simple point charge extended (SPCE) water model. To ensure charge neutrality and mimic physiological conditions, 0.15 M $Na+$ and Cl-counterions were added. System preparation protocols were guided by a previously published methodology [35]. After NPT equilibration, the resulting structure was subjected to a 200 ns production run in an NPT ensemble. The simulation trajectory was analyzed using an array of tools provided by the GROMACS software, such as protein root mean square deviation (RMSD), root-mean-square fluctuation (RMSF), radius of gyration (RG), solvent-accessible surface area (SASA), and hydrogen bonding [36]. Additionally, the binding free energy associated with AE was calculated throughout the simulation time using the MM-PBSA method and the GROMACS utility g_mmpbsa [37].

2.2.5. Animals

Healthy adult albino Wistar strains (220–250 g) of both sexes aged 8–10 weeks were obtained from Vyas Lab, Hyderabad. The rats were housed under standard husbandry conditions (25 ± 5 °C, 12 h light/dark cycle) with standard rat feed and water available ad libitum. The experimental protocol was approved by the IAEC of the Santhiram College of Pharmacy (1519/PO/Re/S/l1/CPCSEA/2022/005).

2.2.6. Preparation of AENP

The nanosuspension was formed by dissolving aloe-emodin in 1-butanol to obtain a 15 mg/mL solution, which was combined with an antisolvent (hexane) to produce a nanosuspension. The solvent and antisolvent must be miscible for the successful formation of nanosuspensions. A 1:10 ratio of 1-butanol to n-hexane is acceptable. The nanosuspension was then transferred to a round-bottomed flask and connected to a rotary evaporator. The flask was placed in a bath at 40 °C with a rotation speed of 90 rpm and pressure of 300 mbar. The solid was dried by evaporation to obtain nanoparticles. The prepared nanoparticles were characterized using a HORIBA particle size analyzer (SZ100), which indicated their particle size. The stability of the prepared formulation was characterized using the polydispersity index (PDI) [38].

2.2.7. Experimental procedure for the induction of cerebral ischemia in rats via the BCCAO/R model

Under anesthesia with ketamine (60 mg/kg) and xylazine (10 mg/kg), common carotid arteries were exposed and isolated from surrounding tissues and vagus nerves. The sections were then blocked for 10 min and then reopened for 10 min. This constituted one cycle, and the experiment was repeated three times. After three cycles, pupil dilation, corneal reflexes, limb reflexes, and rectal temperature were monitored. A heating lamp was used to maintain body temperature and prevent hypothermia [39].

2.2.8. Experimental design

The experimental animals were randomly divided into five groups (n = 6) and pretreated for 14 days according to the treatment schedule. Cerebral ischemia was induced using the BCCAO/R model [40]. Based on a previous study [17,41], in this study, a sub-maximum dose of 25 mg/kg AE was selected, and its efficacy was compared with that of 25 mg/kg AENP.

Group I Normal control
Group II Sham control group
Group III Disease Control (BCCAO/R)
Group IV AE (25 mg/kg, p.o.) rats were pretreated for 14 days, and then BCCAO/R was performed.
Group V AENP (25 mg/kg, p.o.) was pretreated for 14 days, and then BCCAO/R

2.2.9. Electrocardiogram (ECG) and electroencephalogram (EEG) monitoring

At the end of reperfusion, the rats were subjected to electrocardiogram (ECG) and electroencephalogram (EEG) monitoring under ketamine (60 mg/kg) and xylazine (9 mg/kg) using Polyrite D (Polygraph Digital, RMS, India). Subcutaneous attachment of the ECG electrodes was performed on the paws and chest of the rats in the supine position. ECG parameters, such as RR, PR, QRS intervals, heart rate, and QTc amplitude, were analyzed for cardiac activity [42]. For EEG monitoring, electrodes were placed on the top and lateral sides of the rat head with a dental ceramic cream. The electrodes were connected to a preamplifier. The rats were placed in a recording chamber or cage with minimal restraint to allow normal behavior. EEG signals were recorded using a data acquisition system.

2.2.10. Tissue biochemical parameters

After conducting the ECG and EEG tests, the rats were euthanized, and their brains and hearts were removed and washed with cold 0.9 % saline. Researchers have subsequently used the TTC staining method to determine the size of cerebral infarction [43]. The brain and heart tissues were homogenized at a concentration of 10 % (w/v) in cold phosphate buffer (0.05 M, pH 7.4), and the resulting homogenates were centrifuged at 1000×*g* for 10 min at 4 °C. The supernatant was used to measure glutathione (GSH) [44], superoxide dismutase (SOD) [45], malondialdehyde (MDA) [46], and myeloperoxidase activity [47].

2.2.11. Histological studies

The sagittal portion of the brain was cut and fixed in 10 % neutral buffered formalin, and the heart was fixed in the same solution. The brain and heart were embedded in paraffin to prepare paraffin sections, and 4-μm-thick sections were cut and stained with hematoxylin and eosin (H&E) for histopathological examination [48].

2.2.12. Statistical methods

The mean ± standard error of the mean (SEM) was calculated for all datasets where a significant difference between the means was observed, and this was determined using one-way analysis of variance (ANOVA) followed by a Dunnett comparison test. Statistical significance was set at $p < 0.05$.

3. Results

3.1. Molecular docking

To confirm the accuracy of the docking method, a redocking study preceded the ligand binding to the MPO active site. Crystallographic analysis identified the compound CCl (2-([3,5-bis(trifluoromethyl)benzyl]amino)-N-hydroxy-6-oxo-1,6-

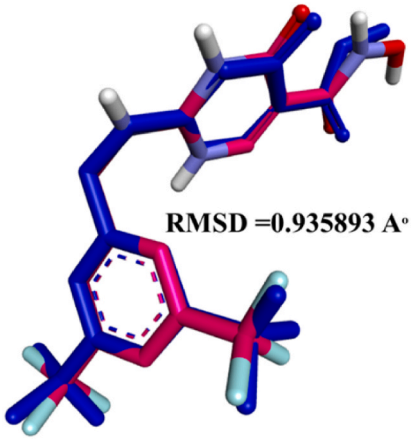

Fig. 1. RMSD values and superimposition of the native cocrystallized (blue) and docked (pink) poses of MPO.

dihydropyrimidinecarboxamide) within the MPO binding pocket. A root mean square deviation (RMSD) of 0.935893 Å between the redocked position and the position observed in the crystal structure (PDB ID: 4c1m) confirmed the reliability and effectiveness of the docking protocol, as depicted in Fig. 1.

Table 1 displays the binding affinity, denoted as ΔG (kcal/mol), of ligands to the target protein, along with the essential amino acids involved in the interaction. Binding affinity quantifies a ligand's propensity to bind a protein; a closer proximity among amino acids involved in binding correlates with a stronger interaction.

The binding energies and interactions between AE and CCl with myeloperoxidase are shown in Table 2. The ligands AE and CCl demonstrated binding affinities of −6.9 and −7.7 ΔG (kcal/mol), respectively. The detailed interactions include various amino acids at specified distances (Å), indicative of hydrogen bonding, as well as hydrophobic and electrostatic interactions. Hydrogen bonding involves GLU A:102 (5.32) and ARG A:424 (4.82), while hydrophobic interactions are mediated by PHE C:407 (8.11) and LEU C:417 (6.42). ARG C333 (6.58, 7.34) engages in electrostatic interactions. In contrast, the interactions for CCl comprised hydrogen bonds with GLN A:91 (5.35), GLU A:242 (4.85) and HIS C:336 (4.46); hydrophobic interactions with ARG C:239 (4.30), VAL C:410 (5.13), PHE A:407 (5.44), MET C:411 (5.87), PRO A:220 (5.13, 7.38) and PHE C:366 (6.21, 6.18); and one electrostatic interaction involving GLU A:242 (4.63) Fig. 2.

3.2. Molecular dynamic studies

All-atom MD simulations can be used to effectively analyze protein structural dynamics and interactions with ligands, revolutionizing the field of computer-aided drug design and discovery. This technique facilitates the examination of molecular systems at the atomic scale. In our study, we utilized MD simulations to capture the dynamic changes in the target protein upon binding to ligands. We calculated several parameters, such as the root-mean-square deviation (RMSD), root-mean-square fluctuation (RMSF), radius of gyration (Rg), solvent accessible surface area (SASA), and intermolecular hydrogen bonding, for both protein–ligand complexes.

We assessed the stability of the protein–ligand complex by analyzing the RMSD trends over time (Fig. 3A) (see Fig. 2). The results revealed that equilibrium was attained within 10 ns, with stable distributions over the course of the simulation. The RMSD values confirmed that the stability exceeded 100 ns for both the standard (CCL) and the ligand ALO. This indicated that these complexes remained consistent and stable throughout the simulation, with average RMSD values of 0.25 and 0.02 nm for CCL and 0.30 and 0.03 nm for AE, respectively, signifying minimal variation.

The RMSF was used to assess individual residue fluctuations and identify flexible regions within the protein, providing insights into ligand-binding effects. Higher RMSF values correspond to loosely ordered loops, while more compact structures such as beta-sheets and alpha-helices exhibit lower RMSFs. The quantified RMSF values for all residues in the CCL and AE complexes (Fig. 3B) had averages of 0.12 and 0.08 nm for CCL and 0.11 and 0.06 nm for AE, respectively, suggesting a negligible influence on the overall RMSF distribution of the complexes.

Using the Rg values tracked over time (Fig. 3C), we examined the dynamic stability and compactness of the CCL and its AE complex. The average Rg values for CCL and AE were 2.37 ± 0.007 nm and 2.35 ± 0.007 nm, respectively, indicating almost identical compact structures within both systems.

SASA analytically determines protein molecule accessibility in a solvent. Therefore, by computing SASA values (Fig. 3D), we determined the impact of AE binding on the target's solvent exposure. The average SASA values for CCL and AE were 248.33 ± 3.9 nm^2 and 255.74 ± 4.3 nm^2, respectively, showing a consistent pattern and the absence of significant fluctuations during the simulation.

Finally, hydrogen bond formation plays a vital role in stabilizing protein–ligand interactions. Time-dependent analysis of hydrogen bonding with AE (Fig. 3E) showed that the docked complex remained stable, supported by two to nine hydrogen bonds with AE throughout the simulation. The average SASA values for CCl and AE were thus found to be 248.33 ± 3.9 nm and 255.74 ± 4.3 nm, respectively. In the simulation, the SASA values maintained fair equilibration and did not exhibit large fluctuations.

The formation of hydrogen bonds is critical for evaluating the stability of protein–ligand interactions. In this study, we investigated the time-dependent behavior of the hydrogen bonds in AE (Fig. 3E). According to our analysis, the docked complex is stable throughout the simulation. It is held in place by two to nine hydrogen bonds with ALO.

3.2.1. MM - PBSA

To ascertain the binding affinity between CCl and AE, we measured the strength of their relative binding to a high-energy protein. Comparison of the CCL and AE binding strengths of the MM-PBSA inhibitors. Over a stable simulation trajectory, we calculated the residue-level contributions to interaction energy, as presented in Table 2.

Table 1
Binding energies and interaction details of AE and CCl with myeloperoxidase.

Ligands	Protein	Binding affinity, ΔG (Kcal/mol)	Amino acids involved and distance (Å)		
			Hydrogen-Bond Interactions	Hydrophobic Interactions	Electrostatic Interactions
AE	MPO (PDB: 4C1M)	−6.9	GLU A:102 (5.32), ARG A:424 (4.82)	PHE C:407 (8.11), LEU C:417 (6.42)	ARG C:333 (6.58, 7.34)
CCl		−7.7	GLN A:91 (5.35), GLU A:242 (4.85), HIS C:336 (4.46)	ARG C:239 (4.30), VAL C:410 (5.13), PHE A:407 (5.44), MET C:411 (5.87), PRO A:220 (5.13, 7.38), PHE C:366 (6.21, 6.18)	GLU DA:242 (4.63)

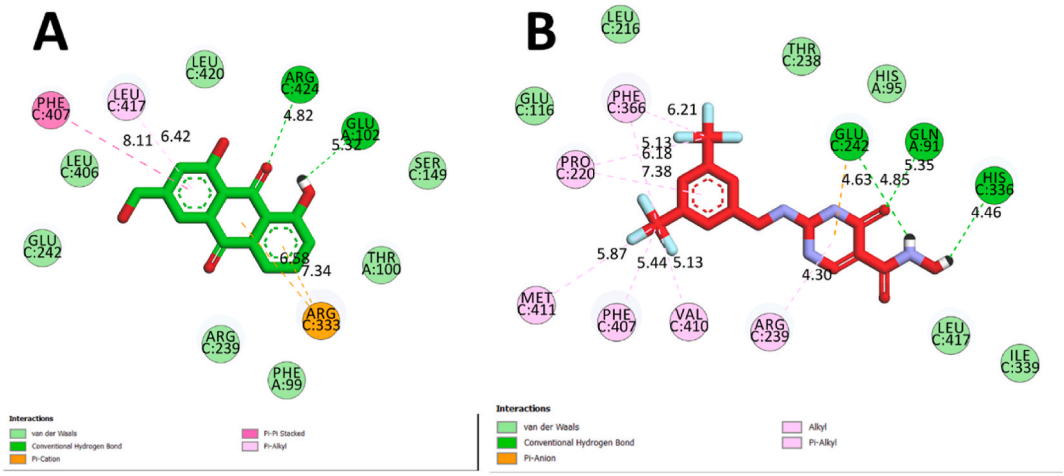

Fig. 2. 2D interactions of selected ligands with MPO. (A) AE (B) CCl (2-{[3,5-bis(trifluoromethyl)benzyl]amino}-*n*-hydroxy-6-oxo-1,6-dihydropyrimidine-5-carboxamide).

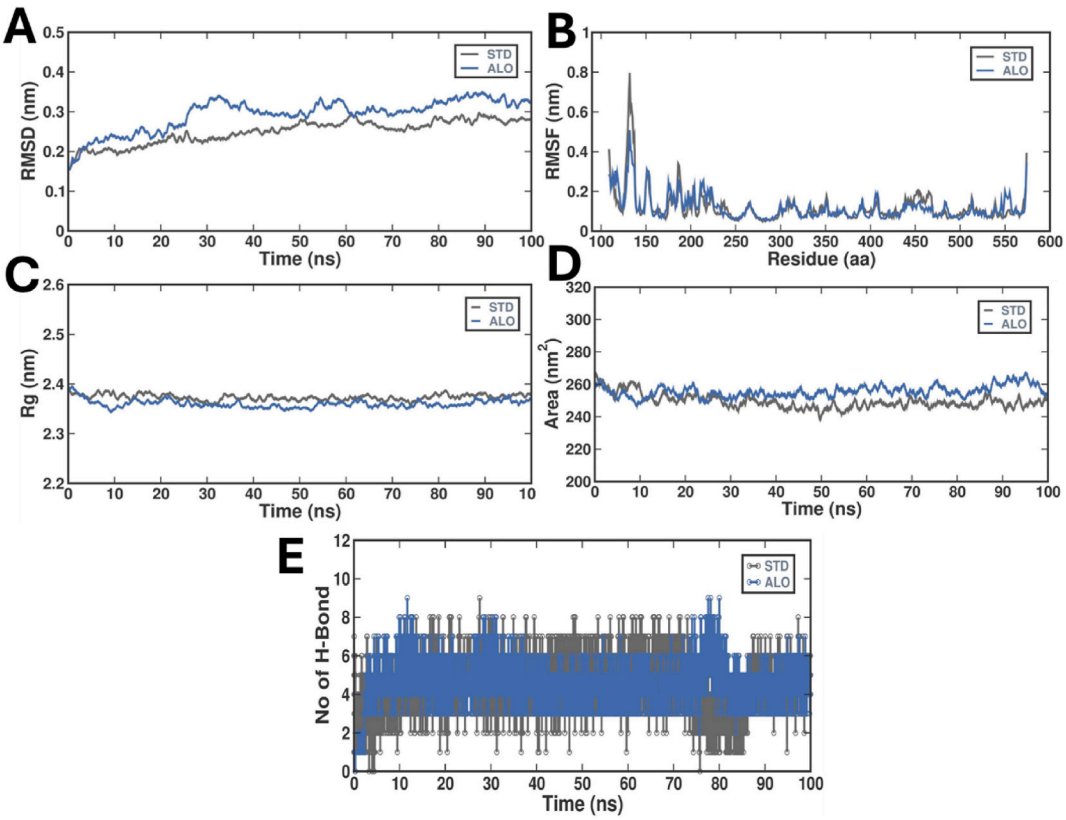

Fig. 3. Molecular simulation plots of AE and CCl with 4C1M. A) RMSD plot; B) RMSF plot; C) Rg plot; D) SASA plot; and E) number of hydrogen bonds over the simulation time.

The molecular interaction energies revealed exciting insights into the different behaviors of CCl and AE. With CCl presenting an elevated van der Waals energy of −112.771 ± 23.244 kJ/mol, over the van der Waals energy of AE of −83.974 ± 14.054 kJ/mol, the former can form stronger dispersion forces, representing relatively stronger intermolecular attraction, compared to the AE. On the other hand, an increasingly higher electrostatic energy of −225.617 ± 10.423 kJ/mol is shown by AE, which suggests that there are more pronounced dipole–dipole or ion-dipole interactions than in CCl. The polar solvation energies for CCl and AE were consistently highly positive at 253.003 ± 70.776 kJ/mol and 267.778 ± 23.634 kJ/mol, respectively, indicating that the molecules had sizeable

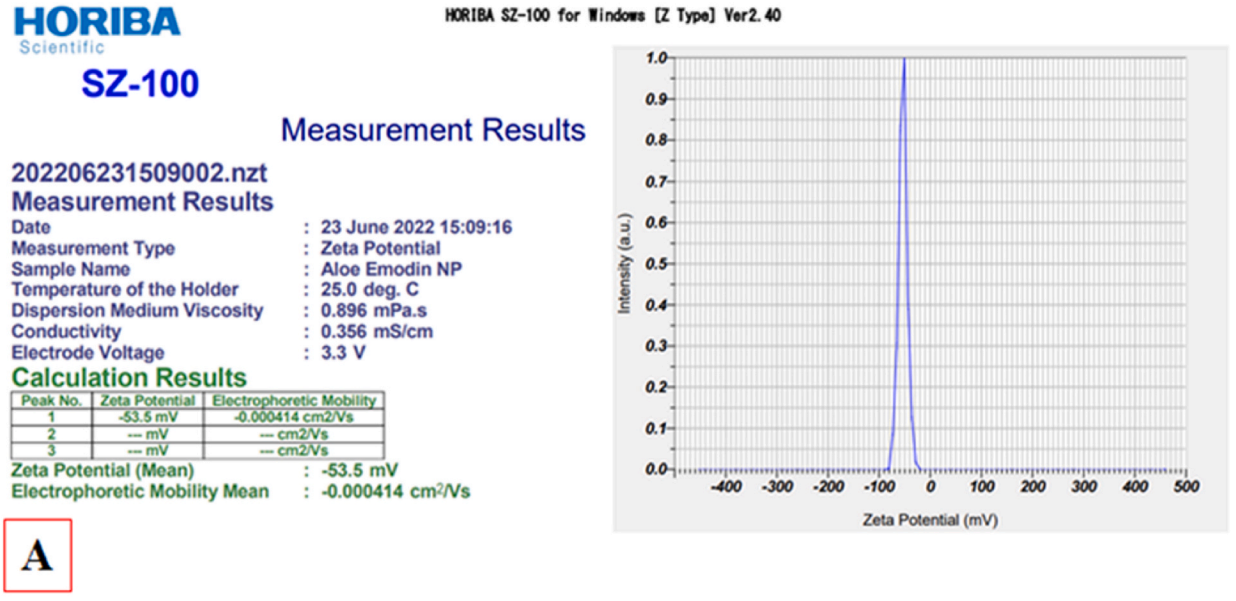

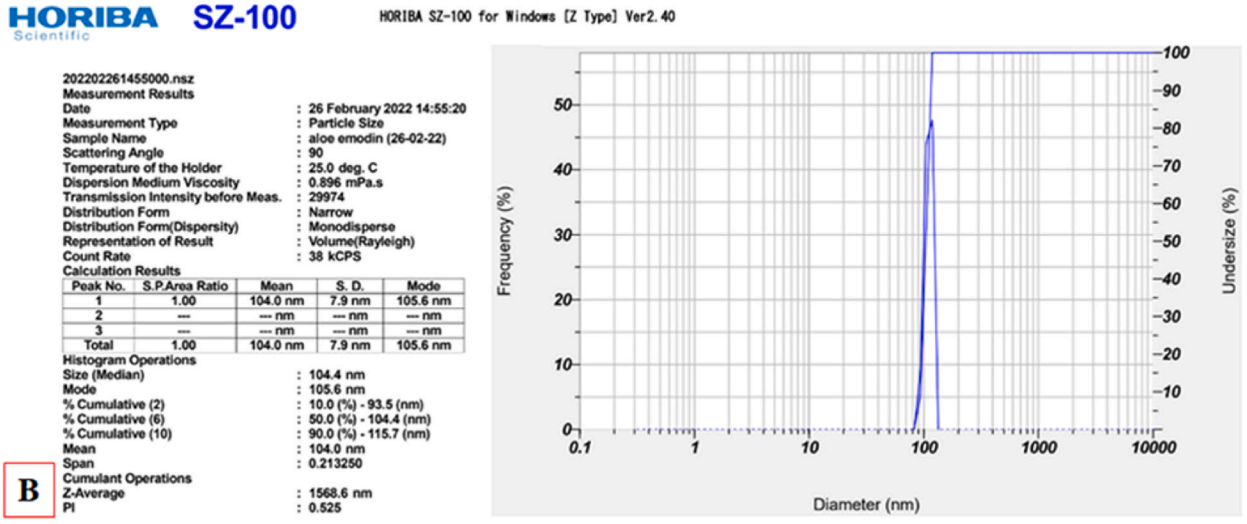

Fig. 4. AENP characterization: A) Particle zeta potential and B) particle size.

Table 2
Binding free energies from MM-PBSA calculations of CCl and AE.

System	van der Waal energy	Electrostatic energy	Polar solvation energy	Binding energy
CCl	−112.771 ± 23.244 kJ/mol	−146.272 ± 27.497 kJ/mol	253.003 ± 70.776 kJ/mol	−22.793 ± 30.727 kJ/mol
AE	−83.974 ± 14.054 kJ/mol	−225.617 ± 10.423 kJ/mol	267.778 ± 23.634 kJ/mol	−57.137 ± 13.198 kJ/mol

affinities for solvent molecules, with AE showing the highest and most polar solvation affinity. The binding energies also showed negative values for both systems, revealing the binding of both CCl and AE to the 4C1M surface. Compared with AE, CCl has more vital binding interactions with the 4C1M surface (−22.793 ± 30.727 kJ/mol compared to −57.137 ± 13.198 kJ/mol). These molecular results concisely illustrate the molecular behavior of CCl and AE with 4C1M, particularly the intermolecular interactions.

3.3. AENP characterization

We successfully developed AENPs; shows homogeneous diameter of 104.4 ± 7.9 nm and a polydispersity index of 0.525–0.586. The prepared nanoparticles exhibited a zeta potential of −53.5 mV, indicating the stability of the prepared nanoparticles [Fig. 4 (A, B)]

3.4. Effect of cerebral infarction on BCCAO/R rats

The current study showed a remarkable increase (52.21 %, $p < 0.001$***) in the percentage of cerebral infarction in BCCAO/R rats compared to that in normal control rats. The percentage of cerebral infarction area decreased in the AENP (13.96 %; $p < 0.001$***)-treated rats compared to that in the AE (26.65 %; $p < 0.01$**)-treated rats [Fig. 5 (A-E), 8A].

3.5. Effect of AENP on EEG

Compared with those in the normal and sham groups, rats subjected to BCCAO/R exhibited high-amplitude unsynchronized polyspikes. A previous study reported that stroke rat EEG showed polyspikes and unsynchronized waves; similar results were observed in stroke rats [49]. EEG revealed fewer multiple unsynchronized polyspikes and greater amplitudes in AENP-treated BCCAO/R rats than in AE- and BCCAO/R-treated rats [Fig. 6 (A-E)] (see Fig. 7a).

3.6. Effect of AENP on ECG

Compared with the normal group, the BCCAO/R group displayed a significant increase in RR intervals (0.27 ± 0.006; $p < 0.001$ ***), a decrease in PR intervals (0.06 ± 0.006; $p < 0.05$*), a decrease in QRS intervals (0.05 ± 0.012; $p < 0.001$ ***), a decrease in QTc amplitude (0.02 ± 0.011; $p < 0.001$ ***), and a decrease in heart rate (218.21 ± 0.22; $p < 0.001$ ***). In contrast, compared with those in the BCCAO/R and AE treatment groups, the rats that were pretreated with 25 mg/kg AENP exhibited a significant decrease in the RR interval (0.27 ± 0.004; $p < 0.01$*) [Fig. 7b. (A)], an increase in the PR interval (0.1 ± 0.018; $p < 0.05$*) [Fig. 7b. (B)], an increase in the QRS interval (0.12 ± 0.003; $p < 0.001$ ***) [Fig. 7b. (C)], an increase in the QTc amplitude (0.05 ± 0.011; $p < 0.05$*) [Fig. 7b. (D)], and an increase in the heart rate (249 ± 0.096; $p < 0.01$**) [Fig. 7b. (E)].

3.7. Effect of AENP on brain biochemical parameters in BCCAO/R rats

Brain GSH levels were significantly decreased to 0.79 ± 0.456 ($p < 0.001$ ****) in rats with BCCAO/R-induced brain damage compared to those in normal rats (2.11 ± 0.751) and sham rats (2.13 ± 0.756). AENP-treated rats showed significantly greater brain GSH levels (1.68 ± 0.671; $p < 0.001$ ****) than did AE-treated rats (1.55 ± 0.643; $p < 0.01$ **) (Fig. 8B. Brain CAT levels were significantly decreased to 2.06 ± 0.748 ($p < 0.001$ ****) in BCCAO/R-induced rats compared to those in normal rats (9.98 ± 1.625) and sham rats (9.58 ± 1.601) (Fig. 8C). AENP-treated rats showed significantly greater brain CAT levels (5.93 ± 1.26; $p < 0.001$ ****) than did AE-treated rats (4.62 ± 1.15; $p < 0.001$ ***). Brain SOD levels were significantly decreased to 0.7 ± 0.433 ($p < 0.001$ ****) in BCCAO/R-induced rats compared to those in normal rats (3.63 ± 0.989) and sham rats (3.63 ± 0.989). AENP-treated rats showed significantly greater brain SOD levels (2.49 ± 0.817; $p < 0.001$ ****) than did AE-treated rats (2.03 ± 0.736; $p < 0.01$ **) (Fig. 8D). Brain MDA levels were significantly greater at 0.7 ± 0.433 ($p < 0.001$ ****) in BCCAO/R-induced rats than in normal rats (3.63 ± 0.989) and sham rats (3.63 ± 0.989). Compared with AE-treated rats, AENP-treated rats had significantly greater brain MDA levels (2.49 ± 0.817; $p < 0.01$ **) (2.03 ± 0.736; $p < 0.01$) (Fig. 8E). Brain MPO levels were significantly increased to 0.15 ± 0.15 ($p < 0.001$ ****) in BCCAO/R-induced rats compared to those in normal rats (0.02 ± 0.055) and sham rats (0.02 ± 0.055). AENP-treated rats showed significantly lower brain MPO levels (0.09 ± 0.12; $p < 0.01$ **) than did AE-treated rats (0.14 ± 0.157; $p < 0.05$ *) (Fig. 8F).

3.8. Effect of AENP on heart biochemical parameters in BCCAO/R rats

Heart GSH levels were significantly lower in BCCAO/R-induced rats than in both normal and sham rats, with values of 23.8 ± 2.008 and 42.40 ± 2.65, respectively ($p < 0.001$***). Compared with those in the brains of the AENP-treated rats, the GSH levels in the brains of the AE-treated rats were 40 ± 2.5 and 29.6 ± 2.2, respectively ($p < 0.01$**) (Fig. 9A). Heart CAT levels were also significantly lower in BCCAO/R-induced rats than in normal and sham rats, with values of 22.40 ± 1.9 and 43 ± 2.65, respectively ($p < 0.001$***). AENP-treated rats showed increased CAT levels in the rat brain compared to those in AE-treated rats, with values of 37.8 ± 2.5 and 30.4 ± 2.2, respectively ($p < 0.001$***) (Fig. 9B). Heart SOD levels were significantly lower in BCCAO/R-induced rats than in normal and sham rats, with values of 12.52 ± 1.448 and 24 ± 2.01, respectively ($p < 0.001$***). AENP-treated rats showed increased SOD levels in

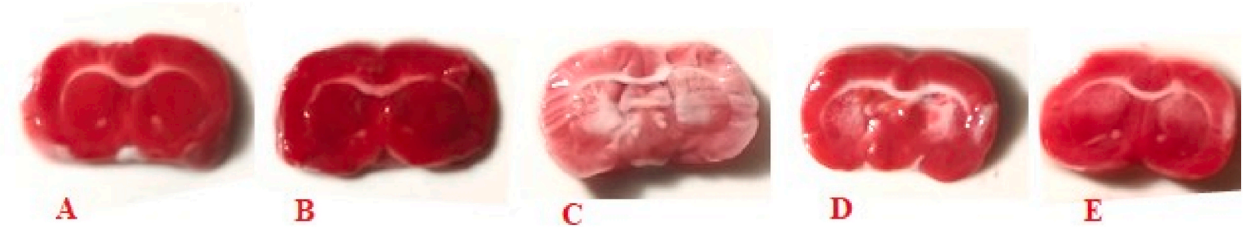

Fig. 5. Effect of AENP on cerebral infarction. A) Normal rats, B) Sham control rats, C) BCCAO/R rats, D) AE treatment + BCCAO/R rats, E) AENP treatment + BCCAO/R rats.

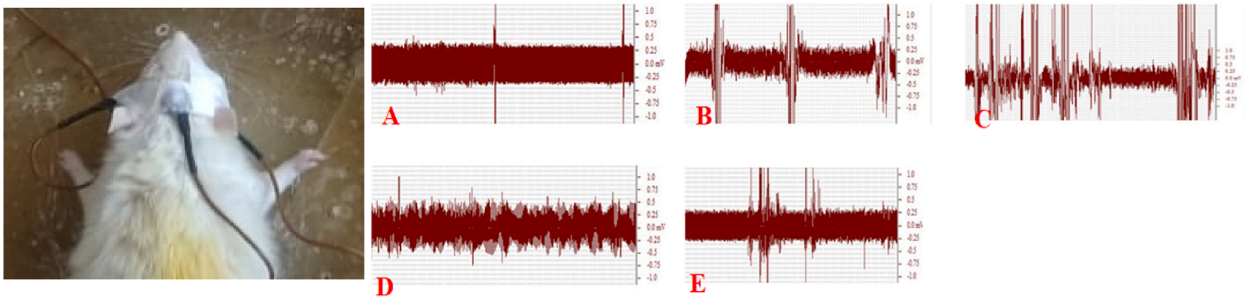

Fig. 6. Effect of AENP on EEG (n = 6; compared with the disease group (Group II), *p < 0.05, **p < 0.01, ***p < 0.001). A) Normal rats B) Sham control C) BCCAO/R rats D) AE treatment + BCCAO/R rats E) AENP treatment + BCCAO/R rats.

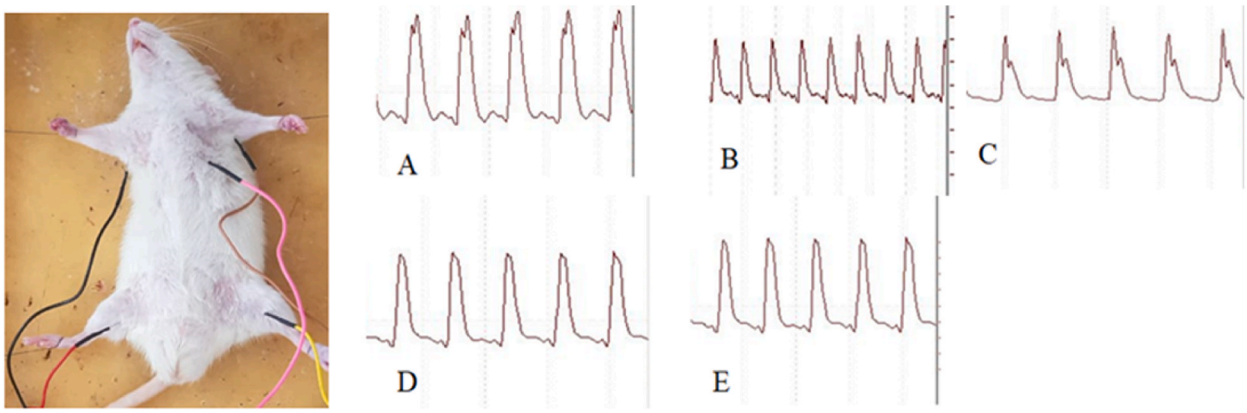

Fig. 7a. Effect of AENP on ECG (n = 6; compared with the disease group (Group II), *p < 0.05, **p < 0.01, ***p < 0.001). A) Normal rats B) Sham Rats C) BCCAO/R Rats D) AE treatment + BCCAO/R Rats D) AENP treatment + BCCAO/R Rats.

the rat brain compared to those in AE-treated rats, with values of 24.52 ± 2.03 and 21.24 ± 1.8, respectively (p < 0.001***) (Fig. 9C). Heart MDA levels were significantly greater in BCCAO/R-induced rats than in normal and sham rats, with values of 7.14 ± 1.09 and 1.52 ± 0.5, respectively (p < 0.001***). Compared with those in the brains of the AENP-treated rats, the MDA levels in the brains of the AE-treated rats were 3.18 ± 0.73 and 5.49 ± 0.96, respectively (p < 0.01**) (Fig. 9D). Heart MPO levels were significantly greater in BCCAO/R-induced rats than in normal and sham rats, with values of 8.53 ± 1.196 and 1.3 ± 0.5, respectively (p < 0.001***). Compared with those in the brains of the AE-treated rats, the MPO levels in the brains of the nano-AENP-treated rats were decreased, with values of 5.1 ± 0.93 and 6.84 ± 1.09, respectively (p < 0.01**) (Fig. 9E)

3.9. Histological studies

3.9.1. Brain histology

Histological analysis indicated that, unlike sham control rats, rats subjected to I/R exhibited shrinkage and atrophy of neurons in the CA1 region of the hippocampus, as well as neuronal necrosis. This finding is consistent with those reported by Vamshi et al. [50]. Compared to BCCAO/R rats, AENP-treated rats exhibited a decrease in the number of scattered neuronal cells, an increase in the number of cells in contact, and a thickening of the pyramidal cell layer in the hippocampal region. Furthermore, compared with AE treatment, AENP treatment resulted in a reduced number of apoptotic neurons and dystrophic changes, as evidenced by the shrinking and irregular shapes of the cells [Fig. 10 (A-E)].

3.9.2. Heart histology

The normal and sham groups displayed a typical appearance of heart tissue without any signs of degeneration or damage. In contrast, the IR group showed an abnormal appearance with wavy myofibers and extensive damage to cardiac muscle fibers and myocytes (yellow arrow), consistent with previous studies [51]. However, AENP administration significantly reduced the extent of histopathological changes induced by IR, resulting in a significant reduction in heart damage. The myocardial fibers in the AENP group were uniformly arranged, and minimal damage to the cardiomyocytes was observed [Fig. 11 (A-E)].

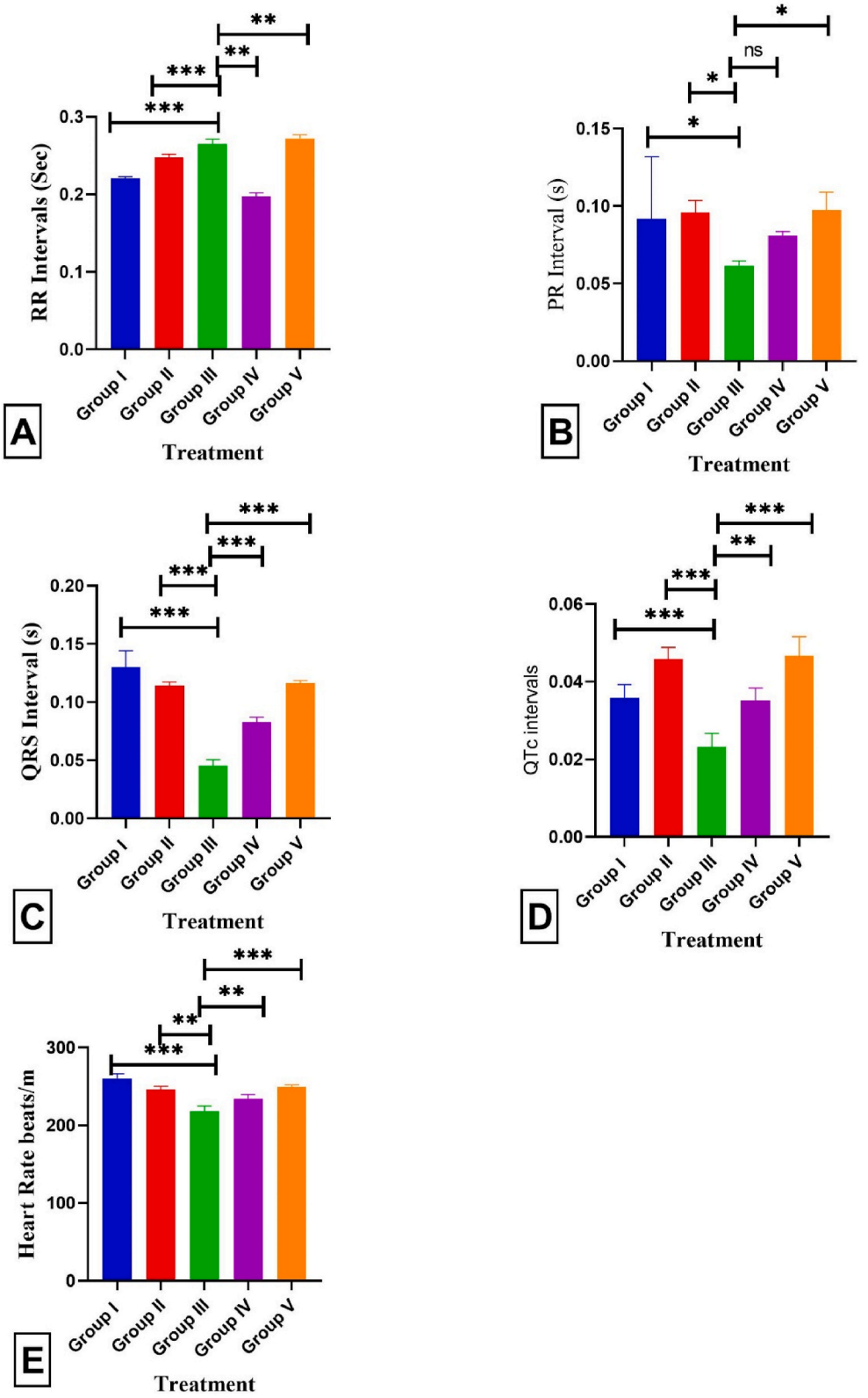

Fig. 7b. Effect on ECG parameters (n = 6; compared with the disease group (Group II), *p < 0.05, **p < 0.01, ***p < 0.001). A) RR intervals. B) PR intervals. C) QRS intervals. D) QTc intervals. E) Heart rate.

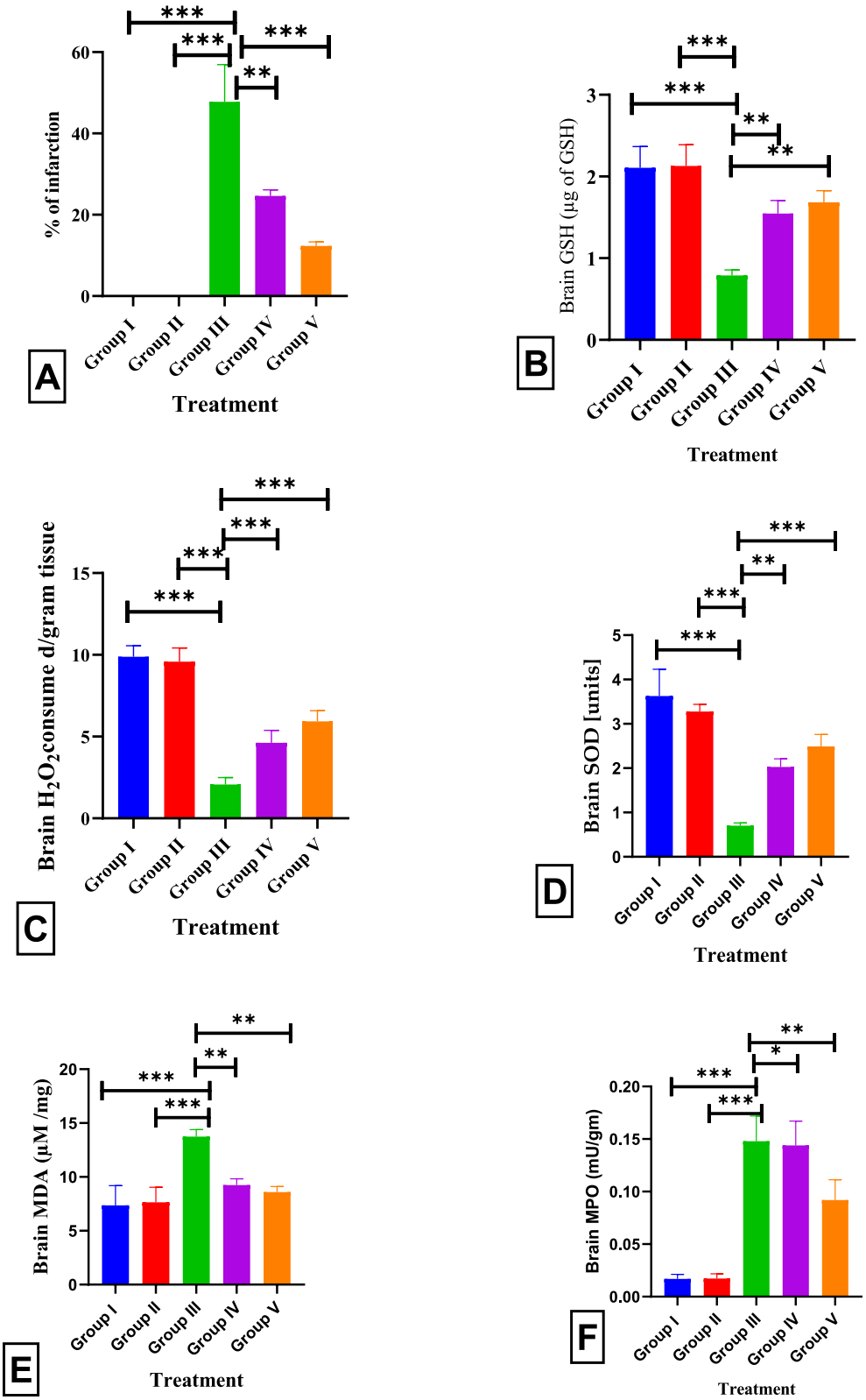

Fig. 8. Effect of AENP on brain biochemical parameters in BCCAO/R rats (n = 6; compared with the disease group (Group II), *p < 0.05, **p < 0.01, ***p < 0.001). A) % infarction size. B) Brain GSH activity. C) Brain CAT activity. D) Brain SOD activity. E) Brain MDA activity. F) Brain MPO activity.

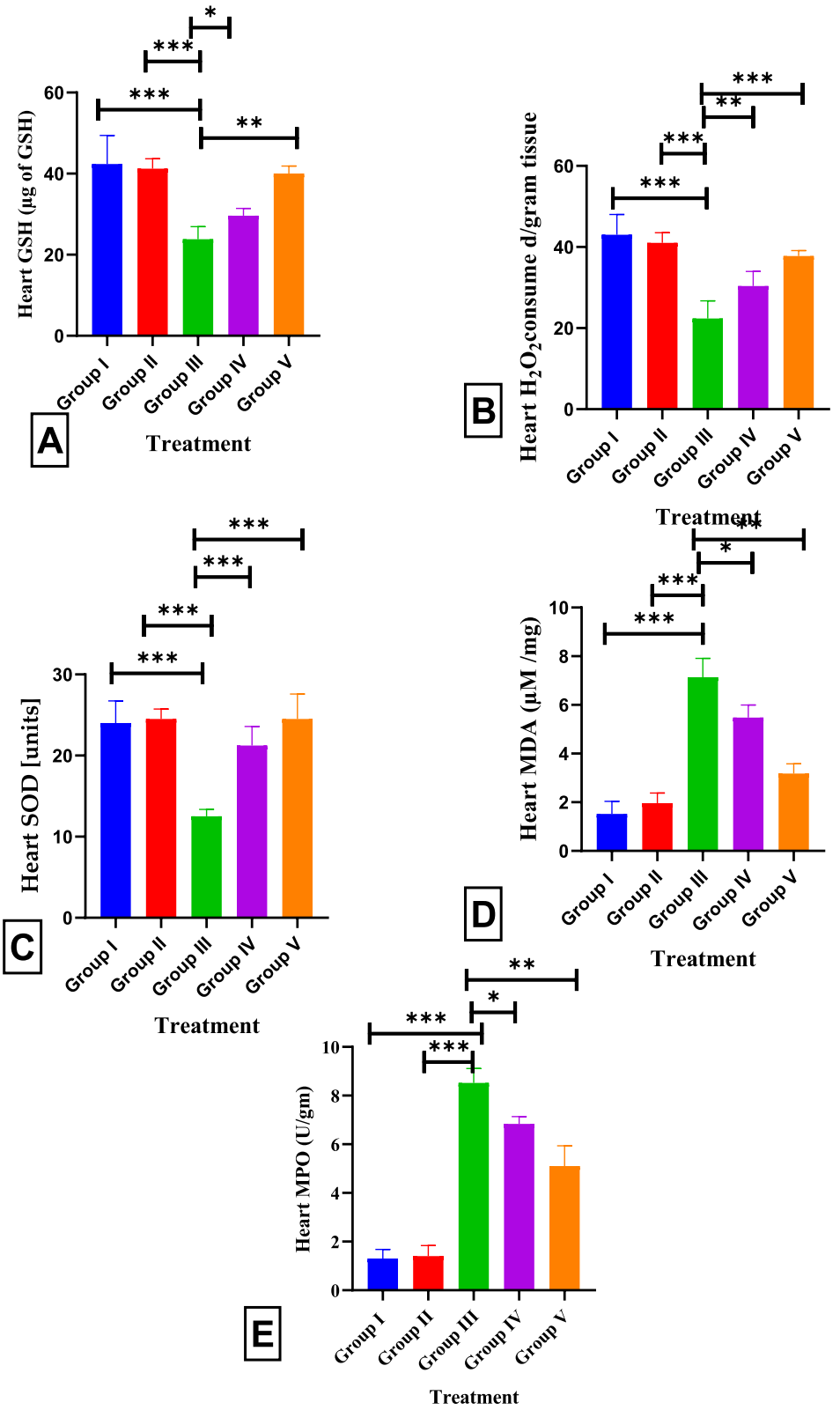

Fig. 9. Effect of AENP on heart biochemical parameters in BCCAO/R rats (n = 6; compared with the disease group (Group II), *p < 0.05, **p < 0.01, ***p < 0.001). A) Heart GSH activity. B) Heart catalase activity. C) Heart SOD activity. D) Heart MDA activity. E) Heart MPO activity.

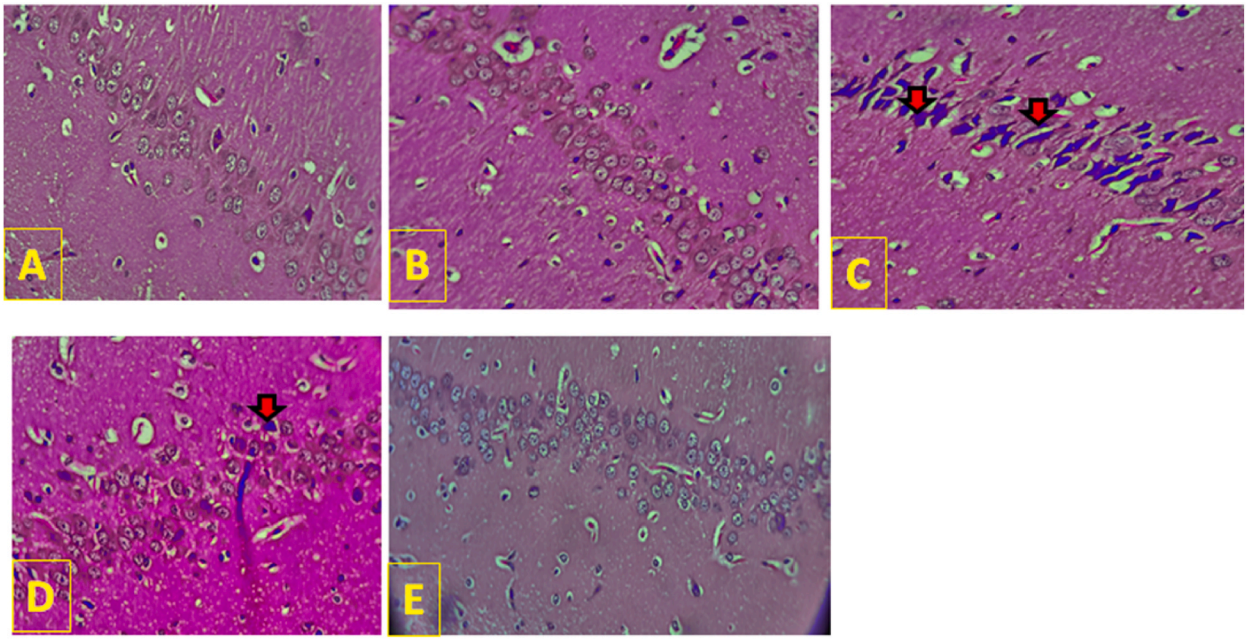

Fig. 10. Displays the histopathological examination results of the CA1 region of the brain hippocampus (compared with the disease group (Group II)). In normal rats, the cell bodies of pyramidal neurons are tightly packed and arranged in 2–3 rows, with small, vesicular nuclei, prominent nucleoli, and minimal cytoplasm (A). The cell body morphology of the sham control group was similar to that of the normal group (B). In contrast, the BCCAO/R rats displayed disarranged and loosely packed cell bodies that appeared dark and elongated and exhibited pyknotic nuclei (C). The AE-treated rats showed well-defined granule cell bodies with some pyknotic nuclei (D). Compared with the AE and BCCAO/R rats, the AENP-treated rats displayed packed, prominent cell bodies with nuclei arranged in 3–4 rows (E). All results are presented in American English, adhering to their spelling, specific terms, and phrases, without making any changes to the citation, reference, or in-line citations or by modifying the numbers in the text.

4. Discussion

Cerebral stroke can lead to secondary myocardial injury, exacerbating outcomes, and increasing mortality. MPO is a pathological factor involved in stroke-associated myocardial injury [52]. AE, a natural anthraquinone compound, exhibits antioxidant and anti-inflammatory effects and can mitigate stroke-induced myocardial damage by inhibiting MPO [12,53]. The therapeutic potential of AE is limited due to its low bioavailability. Using nanotechnology-based delivery systems can circumvent this limitation and enhance the bioavailability of emodin. Using molecular dynamics simulations and in vivo analyses, we showed that aloe-emodin nanoparticles can potentially prevent cerebral stroke-associated myocardial injury by targeting myeloperoxidase. Understanding the protective ability of aloe-emodin nanoparticles could lead to the development of novel therapeutics to mitigate myocardial injury following ischemic stroke.

Molecular docking and MD simulations are indispensable computational modeling techniques in drug discovery pipelines [54]. The former determines how a prospective drug molecule is likely to dock in the binding site of the protein target, predicts the binding affinities, and compares the intermolecular characteristics of the drug-bioactive and bioactive-bioactive sites. The latter methodologies are used to monitor the motion of an atomic and molecular system over time and provide a complete atomic-level understanding of the binding/unbinding and inhibition mechanisms of protein−ligand complexes. Thus, molecular docking and MD simulations can provide accurate structural data on a drug-protein complex's binding energy, stability patterns, and dynamics over time, enabling the delineation of lead optimization and structure-activity relationship (SAR) studies. By harnessing the potential of high-throughput in silico screening coupled with computational techniques that can eliminate atomic-level hints, these methods have led us to succeed in hit identification, lead compound development, and corroboration of the proposed mechanism in a very cost-efficient manner; that is, avoiding the financial and temporal expense of wet laboratory iterations will make it possible to facilitate a swift drug discovery process.

The present study showed a significant binding affinity between AE and CCl: the molecular docking results predicted a binding affinity of −6.9 kcal/mol for AE and −7.7 kcal/mol for CCl. A comparison of these results with those of previous studies was presented to provide more context for the results. Van Antwerpen et al. and Aldib et al. described [55] the design and synthesis of novel bisarylalkyl amine derivatives as potent myeloperoxidase inhibitors that interact with Glu102, Arg424, Gln91, and Arg239. In this study, AE interacted with Glu102 and Arg424 through hydrogen bonds, CCl interacted with Gln91 through hydrogen bonds, and Arg239 interacted via hydrophobic interactions. Matos et al. [56] described the molecular docking of ligands obtained from the zinc database with myeloperoxidase. They reported that ZINC660255 interacts with Glu102 through hydrogen bonding, with Gln91

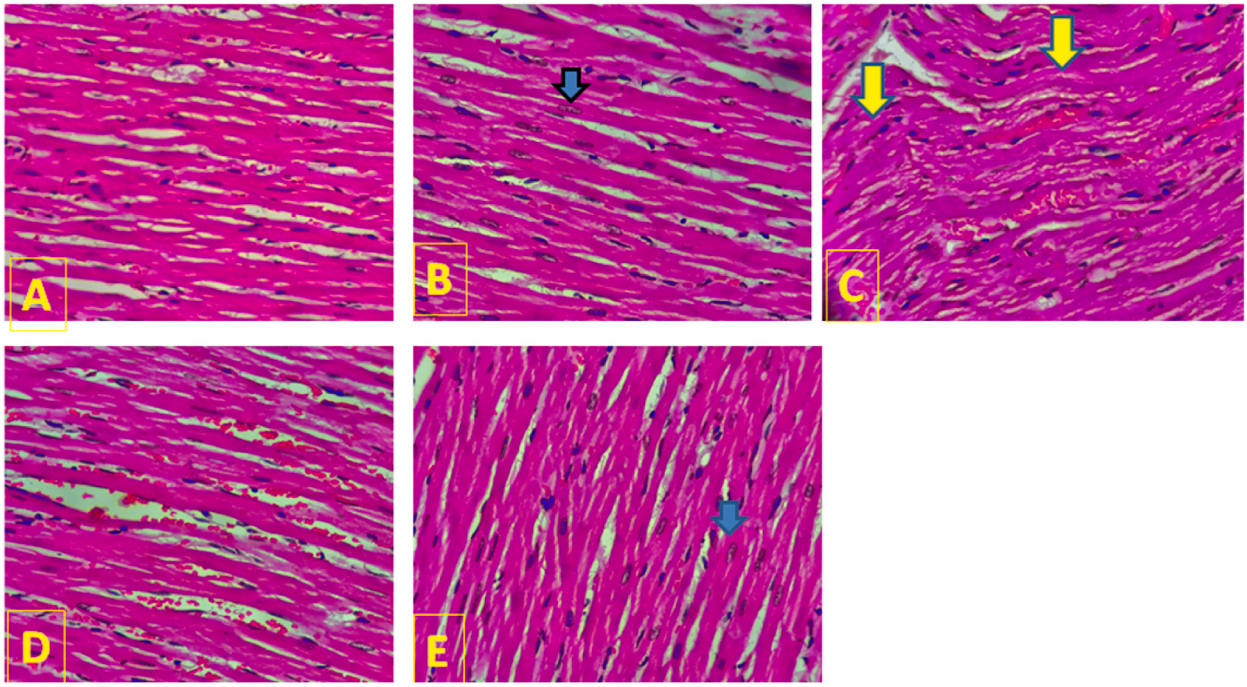

Fig. 11. Histological examination results of the hearts of the rats in the experimental groups (compared with those in the disease group) (group II). A) shows the normal group, which has a standard histological architecture of cardiac myocytes with prominent nuclei. B) represents the sham group, which has a histological architecture of cardiac myocytes similar to that of the normal group. C) shows the BCCAO/R group, which exhibited marked degeneration of cardiac muscle fibers, extensive damage to cardiac myocytes (indicated by the yellow arrow), and wavy myofibers. D) shows the AE treatment group, which exhibited damage to cardiac myocytes and a few cardiac myocytes with prominent nuclei. E) shows the AENP treatment group, which exhibited compact, uniformly arranged myocardial fibers with uniformly and prominently placed nuclei (indicated by the blue arrow).

through d π-stacking interactions, and that ZINC4471880 interacts with Gln91 through hydrogen bonding. This finding suggested that AE is a potent MPO inhibitor owing to these interactions, which are essential for MPO inhibition.

MD simulations were performed to determine the dynamic stability of the ligand–protein complexes for all complexes according to standard protocols. Trajectory analysis revealed that the RMSD of the protein backbone atoms stabilized at 3 Å over 20 ns, indicating that the protein structure was stable [57]. The RMSF showed that the loop regions had some fluctuations, and the loop sites were unshaken (rigid). The compaction of the complex is shown in the radius of gyration (Rg) plot. The minimal SASA indicated that no solvent exposure would lead to instability throughout the MD simulation study. Hydrogen bond analysis revealed that the ligands unfolded to the native conformation, as there was a critical intermolecular hydrogen bond, and the binding interactions remained similar to those in the initial conformation. The Molecular Mechanics/Poisson-Boltzmann Surface Area (MM-PBSA) simulation method was applied to predict the binding's molecular target protein-free energies, the presence of correct complexes, and the validation of binding tutorial results. It was concluded that alloconazole and isocladosporin showed stable conformations throughout the 100 ns simulations and RMSD, RMSF, RG, and SASA [58].

Table 2 displays the binding affinities of the molecular dynamics methods for the CCl and AE systems. The van der Waals interaction energy, which is responsible for nonbonded interactions, is negative for both ligand molecules, but CCl displays stronger hydrophobicity than does AE. In addition, the electrostatic energy is negative, implying favorable electrostatic interactions between the ligands' charged groups and the active site's respective residues. Overall, by comparing the binding energies of AE and CCl determined using the MM-PBSA method, it can be inferred that AE is stronger than CCl, with values of -57.137 ± 13.198 and -22.793 ± 30.727 kJ/mol, respectively. This finding validates the docking data, confirming that AE has better binding ability. MD analysis was used to elucidate the molecular mechanisms involved in the interactions between ligands and receptors.

Multiple organ dysfunction syndrome occurs in approximately 11.5 % of patients diagnosed with acute cerebrovascular disorders, accounting for 40.3 % of deaths [59]. Ischemic stroke leads to oxidative harm to tissues, which is exacerbated by reperfusion, an essential process for sustaining ischemic tissues and producing ischemia–reperfusion (I/R) damage. The occurrence of cardiac oxidative stress resulting from cerebral I/R shows that damage to the heart can impact the brain, and vice versa. Empirical and medical research indicates that oxidative stress could impact the correlation between brain impairment and heart dysfunction [60]. This study highlighted the significant impact of oxidative stress on the disruption of brain-cardiac control, which might result in long-term health complications as well as mortality following stroke. Cardiac problems rank as the second most prevalent cause of mortality following stroke. Acute ischemic stroke has been shown to produce both acute and persistent decreases in heart function in people without previous cardiac disease [59]. Our findings suggest that oxidative stress may serve as a pathway for harmful brain-heart connections

following stroke. Antioxidants have shown potential in stroke treatment by counteracting free radicals and safeguarding essential organs from I/R damage [61]. The potential use of medicinal plants for the treatment of nonneurological dysfunction caused by cerebral I/R injury has not been well researched. However, peripheral organ failure may contribute to systemic nonneurological problems following stroke in clinical settings [59]. There is a lack of information regarding the impact of cerebral ischemia-induced oxidative stress on nonneurological organs. AE has not been evaluated for its capacity to protect distant organs from oxidative damage caused by ischemic stroke, despite its purported antioxidant and neuroprotective properties. The BCCAO/R paradigm was used to induce cerebral ischemia in rats, and its effect on oxidative stress in nonneurologically distant organs, specifically the heart, was examined. The study revealed that BCCAO/R leads to an elevation in oxidative stress levels in the heart. The limited bioavailability of AE restricts its therapeutic use [24,62]. The limited bioavailability of AE restricts its therapeutic use [24,62]. Zeta potential, a measure of electrostatic charge, is often the most important factor controlling the behavior of suspended particles. For example, a negative zeta potential means that the surfaces of the particles tend to be covered by negatively charged groups, most often due to the ionization of acidic groups or the adsorption of anions. A negative charge typically causes repulsion between particles and, at least partially, prevents them from sticking together [63]. This makes them easier to suspend and more stable. Normally, particles with a zeta potential greater than −30 mV are considered to be very stable. For example, when developing drug delivery systems, such as nanoparticles, we often want the particles to interact in a specific way with the biological membranes and cells in our body. Therefore, a negative zeta potential might result in different interactions with biological membranes and cells because of this charge. This, in turn, might affect the drug's cellular uptake, where the drug is released in the body, and its overall efficacy. The zeta potential also modulates the release profile of drugs from the particles. A negative zeta potential can increase the stability of the particle surface in normal biological fluid and make it easier for the drug to be detected by the immune system. Therefore, in the present study, we synthesized AENP and tested their therapeutic potential by comparing their efficacy with that of AE against BCCAO/R-induced oxidative stress in the heart.

GSH and CAT are essential low-molecular-weight antioxidants produced by cells, among which GSH is the most prevalent and important (Forman et al., 2009). The depletion of GSH, CAT, and SOD implies the accumulation of peroxides in the heart, as reported previously [64,65]. The marked reduction in GSH, SOD, and CAT activities in the heart and brain and their reversal by AENP in the present study confirmed BCCAO/R-induced oxidative stress in the heart and the antioxidant properties of AE [66]. The end product of lipid peroxidation, MDA, generates high levels of ROS that are capable of damaging cells, as observed in neurological diseases. The increase in lipid peroxidation in the hearts of rats after BCCAO/R found in this study agrees with earlier reports demonstrating elevated lipid peroxidation in the brain following BCCAO/R [64]. A significant decrease in lipid peroxidation following BCCAO/R was observed in the organs studied, which may be indicative of the defensive effect of AENP against lipid peroxidation and oxidative insult in the heart induced by cerebral ischemia/reperfusion (I/R), which is known to possess potent antioxidant and protective properties.

MPO allows the progression of inflammatory conditions by promoting tissue damage. It accelerates the oxidation of hydrogen peroxide (H2O2), leading to the generation of reactive chlorinating substances such as hypochlorous acid (HOCl). These substances can then react with electron-rich components in various biomolecules [67]. This study revealed that BCCAO/R increased MPO activity in heart. This finding aligns with previous findings of elevated MPO levels in the brain as a result of BCCAO/R [64]. The ability of AENPs to reduce elevated MPO activity in organs indicates their potential for protection against cardiac oxidative damage. MPO causes neuroinflammation that involves various biological mediators and signalling cascades. In ischemic brain damage, the PI3K/AKT signaling pathway is involved in the cellular signaling process that occurs during MPO-mediated inflammation. The current study focused on estimating the expression of MPO in brain and heart tissue. Our future research will focus on investigating the PI3K/AKT signalling pathway in stroke and stroke-associated cardiac PI3K/AKT signalling pathways.

5. Conclusion

According to our computational analysis, AE clearly inhibited MPO more strongly than CCl. Cerebral ischemia/reperfusion resulted in notable oxidative damage, whereas AENPs demonstrated strong posttreatment defense against oxidative stress caused by BCCAO/R. The present study provides initial evidence of the capacity of AENP to mitigate poststroke oxidative stress in the heart. These findings indicate that AENP has potential as a phytomedicinal agent for mitigating postischemic heart dysfunction and reducing mortality rates.

Ethics statement

The Institutional Animal Ethics Committee of the Santhiram College of Pharmacy approved all the experimental protocols involving albino Wistar rats (Approval No. 1519/PO/Re/S/l1/CPCSEA/2022/005).

Funding

This research was funded by King Saud University, Riyadh, Saudi Arabia, Project Number (RSPD2024R709).

CRediT authorship contribution statement

Praveen Kumar Pasala: Writing – review & editing, Writing – original draft, Validation, Project administration, Methodology, Investigation, Formal analysis, Data curation, Conceptualization. **Niranjan Kumar Raghupathi:** Resources, Formal analysis, Data curation. **Deepak A. Yaraguppi:** Formal analysis, Data curation. **Ranadheer Reddy Challa:** Formal analysis, Conceptualization.

Bhaskar Vallamkonda: Methodology, Formal analysis, Data curation. **Sheikh F. Ahmad:** Writing – review & editing, Supervision, Project administration, Funding acquisition. **Yeswanth Chennamsetty:** Formal analysis. **P.V. Kamala Kumari:** Validation, Methodology. **Prasanth DSNBK:** Writing – review & editing, Writing – original draft, Visualization, Software, Formal analysis, Data curation.

Declaration of competing interest

The authors declare that they have no known competing financial interests or personal relationships that could have appeared to influence the work reported in this paper.

Acknowledgments

The authors acknowledge and extend their appreciation to the Researchers Supporting Project Number (RSPD2024R709), King Saud University, Riyadh, Saudi Arabia, for funding this study.

DST-FIST Lab, Raghavendra Institute of Pharmaceutical Education & Research- Autonomous, Anantapur, India for providing Instrumentation support to carryout research.

References

[1] T. Kalogeris, C.P. Baines, M. Krenz, R.J. Korthuis, Cell biology of ischemia/reperfusion injury, Int Rev Cell Mol Biol 298 (2012) 229–317, https://doi.org/10.1016/B978-0-12-394309-5.00006-7.

[2] J.W. Thompson, S. Narayanan, M.A. Pérez-Pinzón, Redox signaling pathways involved in neuronal ischemic preconditioning, Curr. Neuropharmacol. (2012), https://doi.org/10.2174/1570159x11209040354.

[3] M. Yang, J. Chen, J. Zhao, M. Meng, Etanercept attenuates myocardial ischemia/reperfusion injury by decreasing inflammation and oxidative stress, PLoS One (2014), https://doi.org/10.1371/journal.pone.0108024.

[4] S.S. Xie, W. Deng, J. Chen, Q. Wu, H. Li, J. Wang, W. Li, C. Liu, M. Duan, Z. Cai, Q. Xie, T. Hu, X. Zeng, Q.Z. Tang, Andrographolide protects against adverse cardiac remodeling after myocardial infarction through enhancing Nrf2 signaling pathway, Int. J. Biol. Sci. (2020), https://doi.org/10.7150/ijbs.37269.

[5] G. Ying, Z. Tang, J. Zhang, J. Zeng, Z. Zheng, W. Zhang, L. Ding, T.-C. Wen, D. Yi, Long noncoding RNA CASC2 protect ROS-induced oxidative stress in myocardial infarction by miR-18a/SIRT2, Biotechnol. Appl. Biochem. (2021), https://doi.org/10.1002/bab.2252.

[6] K. Thiankhaw, N. Chattipakorn, The effects of hyperbaric oxygen therapy on the brain with middle cerebral artery occlusion, J. Cell. Physiol. (2020), https://doi.org/10.1002/jcp.29955.

[7] X.-T. Su, L. Wang, S.M. Ma, Y. Cao, N. Yang, L.-L. Lin, M. Fisher, J.W. Yang, C.Z. Liu, Mechanisms of acupuncture in the regulation of oxidative stress in treating ischemic stroke, Oxid. Med. Cell. Longev. (2020), https://doi.org/10.1155/2020/7875396.

[8] R. Deng, X. Hua, J. Li, W. Chi, Z. Zhang, F. Liu, L. Zhang, S.C. Pflugfelder, D. Li, Oxidative stress markers induced by hyperosmolarity in primary human corneal epithelial cells, PLoS One (2015), https://doi.org/10.1371/journal.pone.0126561.

[9] S. Chen, H. Chen, Q. Du, J. Shen, Targeting myeloperoxidase (MPO) mediated oxidative stress and inflammation for reducing brain ischemia injury: potential application of natural compounds, Front. Physiol. (2020), https://doi.org/10.3389/fphys.2020.00433.

[10] C.-L. Phuah, T. Dave, R. Malik, M.R. Raffeld, A. Ayres, J.N. Goldstein, A. Viswanathan, S.M. Greenberg, J. Jagiełła, B.M. Hansen, B. Norrving, J. Jimenez-Conde, J. Roquer, A. Pichler, C. Enzinger, J. Montaner, I. Fernandez-Cadenas, A. Lindgren, A. Slowik, R. Schmidt, A. Biffi, N.S. Rost, C.D. Langefeld, H.S. Markus, B. D. Mitchell, B. Worrall, S.J. Kittner, D. Woo, M. Dichgans, J. Rosand, C. Anderson, Genetic variants influencing elevated myeloperoxidase levels increase risk of stroke, Brain (2017), https://doi.org/10.1093/brain/awx220.

[11] I.S. Putri, T.N. Robbani, D. Divamillenia, O.G. Pratiwi, R. I'Tishom, Potential Neurogenesis and Neuroprotective Effects of Epigallocatechin-3-Gallate (EGCG) in Green Tea (Camellia Sinensis) through Microglia M2 Induction Process and NLRP3 Inhibition as an Innovation for Ischemic Stroke Adjuvant Therapy: A Review, International Journal of Research Publications, 2021, https://doi.org/10.47119/ijrp100921120222656.

[12] Y. Yu, H. Liu, D. Yang, F. He, Y. Yuan, J. Guo, J. Hu, J. Yu, X. Yan, S. Wang, Z. Du, Aloe-emodin attenuates myocardial infarction and apoptosis via up-regulating miR-133 expression, Pharmacol. Res. 146 (2019) 104315, https://doi.org/10.1016/j.phrs.2019.104315.

[13] J.Y. Yao, L.Y. Lin, X.M. Yuan, W.L. Ying, Y. Xu, X.Y. Pan, G.J. Hao, J.Y. Shen, J.C. Wu, T. Ye, Antifungal activity of rhein and aloe-emodin from rheum palmatum on fish pathogenic saprolegnia sp, J. World Aquacult. Soc. 48 (1) (2017) 137–144.

[14] X. Jiang, Y. Liu, G. Zhang, S. Lin, J. Wu, X. Yan, Y. Ma, M. Ma, Aloe-emodin induces breast tumor cell apoptosis through upregulation of miR-15a/miR-16-1 that suppresses BCL2, Evid Based Complement Alternat Med 2020 (2020) 5108298, https://doi.org/10.1155/2020/5108298.

[15] Y. Zhou, R. Wu, F.F. Cai, W.J. Zhou, Y.Y. Lu, H. Zhang, Q.L. Chen, M.Y. Sun, S.B. Su, Development of a novel anti-liver fibrosis formula with luteolin, licochalcone A, aloe-emodin and acacetin by network pharmacology and transcriptomics analysis, Pharm. Biol. 59 (1) (2021) 1594–1606, https://doi.org/10.1080/13880209.2021.1999275.

[16] S. Kumar, M. Yadav, A. Yadav, P. Rohilla, J.P. Yadav, Antiplasmodial potential and quantification of aloin and aloe-emodin in Aloe vera collected from different climatic regions of India, BMC Complement Altern Med 17 (1) (2017) 369, https://doi.org/10.1186/s12906-017-1883-0.

[17] P.K. Pasala, R. Abbas Shaik, M. Rudrapal, J. Khan, M.A. Alaidarous, S. Jagdish Khairnar, A.R. Bendale, V.D. Naphade, R. Kumar Sahoo, J.H. Zothantluanga, S. G. Walode, Cerebroprotective effect of Aloe Emodin: in silico and in vivo studies, Saudi J. Biol. Sci. 29 (2) (2022) 998–1005, https://doi.org/10.1016/j.sjbs.2021.09.077.

[18] B. Arosio, N. Gagliano, L.M. Fusaro, L. Parmeggiani, J. Tagliabue, P. Galetti, D. De Castri, C. Moscheni, G. Annoni, Aloe-Emodin quinone pretreatment reduces acute liver injury induced by carbon tetrachloride, Pharmacol Toxicol. 87 (5) (2000) 229–233, https://doi.org/10.1034/j.1600-0773.2000.d01-79.x.

[19] X. Tang, Y. Zhang, X. Liu, X. Li, H. Zhao, H. Cui, Y. Shi, Y. Chen, H. Xu, Z. Meng, L. Zhao, H. Chen, Z. Wang, M. Zhu, Y. Lin, B. Yang, Y. Zhang, Aloe-emodin derivative produces anti-atherosclerosis effect by reinforcing AMBRA1-mediated endothelial autophagy, Eur. J. Pharmacol. 916 (2022) 174641, https://doi.org/10.1016/j.ejphar.2021.174641.

[20] R. Chen, S. Wang, J. Zhang, M. Chen, Y. Wang, Aloe-emodin loaded solid lipid nanoparticles: formulation design and*in vitro*anti-cancer study, Drug Deliv. (2014), https://doi.org/10.3109/10717544.2014.882446.

[21] P.H. Huang, C.Y. Huang, M.C. Chen, Y.T. Lee, C.H. Yue, H.-Y. Wang, L. H, Emodin and aloe-emodin suppress breast cancer cell proliferation through ER**α**Inhibition, Evid. base Compl. Alternative Med. (2013), https://doi.org/10.1155/2013/376123.

[22] P. Praveen Kumar, K.T. Sunil Kumar, M. Kavya Nainita, A. Sai Tarun, B.G. Raghu Ramudu, K. Deepika, A. Pramoda, C. Yasmeen, Cerebroprotective potential of hesperidin nanoparticles against bilateral common carotid artery occlusion reperfusion injury in rats and in silico approaches, Neurotox. Res. 37 (2) (2020) 264–274, https://doi.org/10.1007/s12640-019-00098-8.

[23] P.K. Pasala, D. Prasanth, M. Rudrapal, R.R. Challa, S.F. Ahmad, B. Vallamkonda, R. B. R, Anti-Parkinson potential of hesperetin nanoparticles: in vivo and in silico investigations, Nat. Prod. Res. (2024) 1–10, https://doi.org/10.1080/14786419.2024.2344740.

[24] Y.Y. Wu, J.H. Zhang, J.H. Gao, Y.S. Li, Aloe-emodin (AE) nanoparticles suppresses proliferation and induces apoptosis in human lung squamous carcinoma via ROS generation in vitro and in vivo, Biochem. Biophys. Res. Commun. 490 (3) (2017) 601–607, https://doi.org/10.1016/j.bbrc.2017.06.084.

[25] S. Chen, H. Chen, Q. Du, J. Shen, Targeting myeloperoxidase (MPO) mediated oxidative stress and inflammation for reducing brain ischemia injury: potential application of natural compounds, Front. Physiol. 11 (2020) 433, https://doi.org/10.3389/fphys.2020.00433.

[26] V.T. Dao, A.I. Casas, G.J. Maghzal, T. Seredenina, N. Kaludercic, N. Robledinos-Antón, F.D. Lisa, R. Stocker, P. Ghezzi, V. Jaquet, A. Cuadrado, H. Schmidt, Pharmacology and clinical drug candidates in redox, Medicine. Antioxidants & Redox Signaling 23 (14) (2015) 1113–1129, https://doi.org/10.1089/ars.2015.6430.

[27] M.J. Davies, C.L. Hawkins, The role of myeloperoxidase in biomolecule modification, chronic inflammation, and disease, Antioxidants Redox Signal. 32 (13) (2020) 957–981, https://doi.org/10.1089/ars.2020.8030.

[28] Y. Kargapolova, S. Geißen, R. Zheng, S. Baldus, H. Winkels, M. Adam, The enzymatic and non-enzymatic function of myeloperoxidase (MPO) in inflammatory communication, Antioxidants 10 (4) (2021) 562, https://doi.org/10.3390/antiox10040562.

[29] M.Y. Park, H.J. Kwon, M.K. Sung, Evaluation of aloin and aloe-emodin as anti-inflammatory agents in aloe by using murine macrophages, Biosci. Biotechnol. Biochem. 73 (4) (2009) 828–832, https://doi.org/10.1271/bbb.80714.

[30] V.M. Almeida, Ê.R. Dias, B.C. Souza, J.N. Cruz, C.B.R. Santos, F.H.A. Leite, R.F. Queiroz, A. Branco, Methoxylated flavonols from Vellozia dasypus Seub ethyl acetate active myeloperoxidase extract: in vitro and in silico assays, J. Biomol. Struct. Dyn. 40 (16) (2022) 7574–7583, https://doi.org/10.1080/07391102.2021.1900916.

[31] O. Trott, A.J. Olson, AutoDock Vina: improving the speed and accuracy of docking with a new scoring function, efficient optimization, and multithreading, J. Comput. Chem. 31 (2) (2010) 455–461, https://doi.org/10.1002/jcc.21334.

[32] M.N.M. Al-Qattan, M.N. Mordi, Development and application of fragment-based de novo inhibitor design approaches against Plasmodium falciparum GST, J. Mol. Model. 29 (9) (2023) 281, https://doi.org/10.1007/s00894-023-05650-0.

[33] S. Singh, U. Bajpai, A.M. Lynn, Structure based virtual screening to identify inhibitors against MurE Enzyme of Mycobacterium tuberculosis using AutoDock Vina, Bioinformation 10 (11) (2014) 697–702, https://doi.org/10.6026/97320630010697.

[34] A.K. Malde, L. Zuo, M. Breeze, M. Stroet, D. Poger, P.C. Nair, C. Oostenbrink, A.E. Mark, An automated force field topology builder (ATB) and repository: version 1.0, J Chem Theory Comput 7 (12) (2011) 4026–4037, https://doi.org/10.1021/ct200196m.

[35] B.S. Gangadharappa, R. Sharath, P.D. Revanasiddappa, V. Chandramohan, M. Balasubramaniam, T.P. Vardhineni, Structural insights of metallo-beta-lactamase revealed an effective way of inhibition of enzyme by natural inhibitors, J. Biomol. Struct. Dyn. 38 (13) (2020) 3757–3771, https://doi.org/10.1080/07391102.2019.1667265.

[36] D. Prasanth, M. Murahari, V. Chandramohan, C. Guntupalli, L.R. Atmakuri, Computational study for identifying promising therapeutic agents of hydroxychloroquine analogues against SARS-CoV-2, J. Biomol. Struct. Dyn. 40 (22) (2022) 11822–11836, https://doi.org/10.1080/07391102.2021.1965027.

[37] D. Prasanth, M. Murahari, V. Chandramohan, S.P. Panda, L.R. Atmakuri, C. Guntupalli, In silico identification of potential inhibitors from Cinnamon against main protease and spike glycoprotein of SARS CoV-2, J. Biomol. Struct. Dyn. 39 (13) (2021) 4618–4632, https://doi.org/10.1080/07391102.2020.1779129.

[38] M. Kakran, N.G. Sahoo, L. Li, Z. Judeh, Fabrication of quercetin nanoparticles by anti-solvent precipitation method for enhanced dissolution, Powder Technol. 223 (2012) 59–64.

[39] P.K. Pasala, R. Abbas Shaik, M. Rudrapal, J. Khan, M.A. Alaidarous, S. Jagdish Khairnar, A.R. Bendale, V.D. Naphade, R. Kumar Sahoo, J.H. Zothantluanga, S. G. Walode, Cerebroprotective effect of Aloe Emodin: in silico and in vivo studies, Saudi J. Biol. Sci. 29 (2) (2022) 998–1005, https://doi.org/10.1016/j.sjbs.2021.09.077.

[40] S. Surapaneni, T. Prakash, M. Ansari, P.M. Manjunath, D. Kotresha, D. Goli, Study on cerebroprotective actions of Clerodendron glandulosumleaves extract against long term bilateral common carotid artery occlusion in rats, Biomed. Pharmacother. 80 (2016) 87–94, https://doi.org/10.1016/j.biopha.2016.02.029.

[41] M. Xian, J. Cai, K. Zheng, Q. Liu, Y. Liu, H. Lin, S. Liang, S. Wang, Aloe-emodin prevents nerve injury and neuroinflammation caused by ischemic stroke via the PI3K/AKT/mTOR and NF-kappaB pathway, Food Funct. 12 (17) (2021) 8056–8067, https://doi.org/10.1039/d1fo01144h.

[42] R.N. Kumar, D. Prasanth, P.G. Midthuri, S.F. Ahmad, A.V. Badarinath, S.K. Karumanchi, R. Seemaladinne, R. Nalluri, P.K. Pasala, Unveiling the cardioprotective power: liquid chromatography-mass spectrometry (LC-MS)-Analyzed neolamarckia cadamba (roxb.) bosser leaf ethanolic extract against myocardial infarction in rats and in silico support analysis, Plants 12 (21) (2023), https://doi.org/10.3390/plants12213722.

[43] J.B. Bederson, L.H. Pitts, M. Tsuji, M.C. Nishimura, R.L. Davis, H. Bartkowski, Rat middle cerebral artery occlusion: evaluation of the model and development of a neurologic examination, Stroke 17 (3) (1986) 472–476, https://doi.org/10.1161/01.str.17.3.472.

[44] G.L. Ellman, Tissue sulfhydryl groups, Arch. Biochem. Biophys. 82 (1) (1959) 70–77, https://doi.org/10.1016/0003-9861(59)90090-6.

[45] Y. Kono, Reprint of: generation of superoxide radical during autoxidation of hydroxylamine and an assay for superoxide dismutase, Arch. Biochem. Biophys. 726 (2022) 109247, https://doi.org/10.1016/j.abb.2022.109247.

[46] H. Ohkawa, N. Ohishi, K. Yagi, Assay for lipid peroxides in animal tissues by thiobarbituric acid reaction, Anal. Biochem. 95 (2) (1979) 351–358, https://doi.org/10.1016/0003-2697(79)90738-3.

[47] J.P. Eiserich, M. Hristova, C.E. Cross, A.D. Jones, B.A. Freeman, B. Halliwell, A. van der Vliet, Formation of nitric oxide-derived inflammatory oxidants by myeloperoxidase in neutrophils, Nature 391 (6665) (1998) 393–397, https://doi.org/10.1038/34923.

[48] J.D. Bancroft, M. Gamble, Theory and Practice of Histological Techniques, Elsevier health sciences, 2008.

[49] C.X. Lu, T. Qiu, Z.F. Liu, L. Su, B. Cheng, Calcitonin gene-related peptide has protective effect on brain injury induced by heat stroke in rats, Exp. Ther. Med. 14 (5) (2017) 4935–4941, https://doi.org/10.3892/etm.2017.5126.

[50] Vamshi, G., P. D. S. N. B. K, A. Sampath, M. Dammalli, P. Kumar, G. B.S, P. K. Pasala, G. Somasekhar, M. C. Challa, R. Alluril, and V. R. Narala, Possible cerebroprotective effect of citronellal: molecular docking, MD simulation and in vivo investigations. J. Biomol. Struct. Dyn. 1-12, doi: 10.1080/07391102.2023.2220025.

[51] N.B. Türkmen, H. Yüce, A. Taşlıdere, Y. Şahin, İ. Ayhan, S. Unüvar, O. Çiftçi, 18β-glycyrrhetinic acid attenuates global cerebral ischemia/reperfusion-induced cardiac damage in C57BL/J6 mice, Brazilian Journal of Pharmaceutical Sciences 58 (2023).

[52] H. Kamel, J.S. Healey, Cardioembolic stroke, Circ. Res. 120 (3) (2017) 514–526, https://doi.org/10.1161/CIRCRESAHA.116.308407.

[53] M.Y. Park, H.J. Kwon, M.K. Sung, Dietary aloin, aloesin, or aloe-gel exerts anti-inflammatory activity in a rat colitis model, Life Sci. 88 (11–12) (2011) 486–492, https://doi.org/10.1016/j.lfs.2011.01.010.

[54] O.M. Salo-Ahen, I. Alanko, R. Bhadane, A.M. Bonvin, R.V. Honorato, S. Hossain, A.H. Juffer, A. Kabedev, M. Lahtela-Kakkonen, A.S. Larsen, Molecular dynamics simulations in drug discovery and pharmaceutical development, Processes 9 (1) (2020) 71.

[55] I. Aldib, M. Gelbcke, J. Soubhye, M. Prévost, P.G. Furtmüller, C. Obinger, B. Elfving, I.C. Alard, G. Roos, C. Delporte, G. Berger, D. Dufour, K. Zouaoui Boudjeltia, J. Nève, F. Dufrasne, P. Van Antwerpen, Novel bis-arylalkylamines as myeloperoxidase inhibitors: design, synthesis, and structure-activity relationship study, Eur. J. Med. Chem. 123 (2016) 746–762, https://doi.org/10.1016/j.ejmech.2016.07.053.

[56] I.d.A. Matos, N.B. da Costa Júnior, F.C. Meotti, Integration of an inhibitor-like rule and structure-based virtual screening for the discovery of novel myeloperoxidase inhibitors, J. Chem. Inf. Model. 60 (12) (2020) 6408–6418, https://doi.org/10.1021/acs.jcim.0c00813.

[57] S. Khan, U. Farooq, M. Kurnikova, Protein stability and dynamics influenced by ligands in extremophilic complexes–a molecular dynamics investigation, Mol. Biosyst. 13 (9) (2017) 1874–1887.

[58] P. K, D.S.N.B.K. Prasanth, M.K.R. Shadakshara, S.F. Ahmad, R. Seemaladinne, M. Rudrapal, P.K. Pasala, Citronellal as a promising candidate for alzheimer's disease treatment: a comprehensive study on in silico and in vivo anti-acetylcholine esterase activity, Metabolites 13 (11) (2023) 1133.

[59] C. Robba, D. Battaglini, C.S. Samary, P.L. Silva, L. Ball, P.R.M. Rocco, P. Pelosi, Ischaemic stroke-induced distal organ damage: pathophysiology and new therapeutic strategies, Intensive Care Med Exp. 8 (Suppl 1) (2020) 23, https://doi.org/10.1186/s40635-020-00305-3.

[60] A. Méloux, Y. Béjot, L. Rochette, Y. Cottin, C. Vergely, Brain-heart interactions during ischemic processes: clinical and experimental evidences, Stroke 51 (2) (2020) 679–686.

[61] Z. Lin, Y. Jiang, P. Yang, L. Sun, D. Lu, A frog antioxidant peptide protects against myocardial ischemia reperfusion injury in rats, Life 13 (1) (2020) 45–53.

[62] N.R. Thimmegowda, C. Park, B. Shwetha, K. Sakchaisri, K. Liu, J. Hwang, S. Lee, S.J. Jeong, N.K. Soung, J.H. Jang, I.J. Ryoo, J.S. Ahn, R.L. Erikson, B.Y. Kim, Synthesis and antitumor activity of natural compound aloe emodin derivatives, Chem. Biol. Drug Des. 85 (5) (2015) 638–644, https://doi.org/10.1111/cbdd.12448.

[63] S. Patil, A. Sandberg, E. Heckert, W.T. Self, S. Seal, Protein adsorption and cellular uptake of cerium oxide nanoparticles as a function of zeta potential, Biomaterials 28 (31) (2007) 4600–4607, https://doi.org/10.1016/j.biomaterials.2007.07.029.

[64] O.B. Ojo, Z.A. Amoo, I.O. Saliu, M.T. Olaleye, E.O. Farombi, A.C. Akinmoladun, Neurotherapeutic potential of kolaviron on neurotransmitter dysregulation, excitotoxicity, mitochondrial electron transport chain dysfunction and redox imbalance in 2-VO brain ischemia/reperfusion injury, Biomed. Pharmacother. 111 (2019) 859–872, https://doi.org/10.1016/j.biopha.2018.12.144.

[65] L.L. Nwidu, E. Elmorsy, Y.I. Oboma, W.G. Carter, Hepatoprotective and antioxidant activities of Spondias mombin leaf and stem extracts against carbon tetrachloride-induced hepatotoxicity, Journal of Taibah University Medical Sciences 13 (3) (2018) 262–271.

[66] Y. Chen, B. Feng, Y. Yuan, J. Hu, W. Zhao, H. Jiang, W. Li, Z. Fan, Z. Du, Aloe emodin reduces cardiac inflammation induced by a high-fat diet through the TLR4 signaling pathway, Mediators Inflamm 2020 (2020) 6318520, https://doi.org/10.1155/2020/6318520.

[67] S.J. Nicholls, S.L. Hazen, Myeloperoxidase and cardiovascular disease, Arterioscler. Thromb. Vasc. Biol. 25 (6) (2005) 1102–1111, https://doi.org/10.1161/01.ATV.0000163262.83456.6d.